International Journal of Nanomedicine

Dovepress
open access to scientific and medical research

Open Access Full Text Article

ORIGINAL RESEARCH

The Pimpled Gold Nanosphere: A Superior Candidate for Plasmonic Photothermal Therapy

This article was published in the following Dove Press journal:
International Journal of Nanomedicine

Behzad Nasseri[1–3]
Mustafa Turk[4]
Kemal Kosemehmetoglu[5]
Murat Kaya[2]
Erhan Piskin[1]
Navid Rabiee[6]
Thomas J Webster[7]

[1]Chemical Engineering Department, Bioengineering Division and Bioengineering Centre, Hacettepe University, Ankara 06800, Turkey; [2]Chemical Engineering and Applied Chemistry Department, Atilim University, Ankara 06830, Turkey; [3]Bioscience Faculty, Shahid Beheshti University, Tehran, Iran; [4]Bioengineering Department, Kirikkale University, Kirikkale, Turkey; [5]Department of Pathology, Hacettepe Medical Science University, Ankara, Turkey; [6]Department of Chemistry, Shahid Beheshti University, Tehran, Iran; [7]Department of Chemical Engineering, Northeastern University, Boston, MA 02115, USA

Background: The development of highly efficient nanoparticles to convert light to heat for anti-cancer applications is quite a challenging field of research.

Methods: In this study, we synthesized unique pimpled gold nanospheres (PGNSs) for plasmonic photothermal therapy (PPTT). The light-to-heat conversion capability of PGNSs and PPTT damage at the cellular level were investigated using a tissue phantom model. The ability of PGNSs to induce robust cellular damage was studied during cytotoxicity tests on colorectal adenocarcinoma (DLD-1) and fibroblast cell lines. Further, a numerical model of plasmonic (COMSOL Multiphysics) properties was used with the PPTT experimental assays.

Results: A low cytotoxic effect of thiolated polyethylene glycol (SH-PEG$_{400}$-SH-) was observed which improved the biocompatibility of PGNSs to maintain 89.4% cell viability during cytometry assays (in terms of fibroblast cells for 24 hrs at a concentration of 300 µg/mL). The heat generated from the nanoparticle-mediated phantom models resulted in $\Delta T=30°C$, $\Delta T=23.1°C$ and $\Delta T=21°C$ for the PGNSs, AuNRs, and AuNPs, respectively (at a 300 µg/mL concentration and for 325 sec). For the in vitro assays of PPTT on cancer cells, the PGNS group induced a 68.78% lethality (apoptosis) on DLD-1 cells. Fluorescence microscopy results showed the destruction of cell membranes and nuclei for the PPTT group. Experiments further revealed a penetration depth of sufficient PPTT damage in a physical tumor model after hematoxylin and eosin (H&E) staining through pathological studies (at depths of 2, 3 and 4 cm). Severe structural damages were observed in the tissue model through an 808-nm laser exposed to the PGNSs.

Conclusion: Collectively, such results show much promise for the use of the present PGNSs and photothermal therapy for numerous anti-cancer applications.

Keywords: plasmonic, photothermal therapy, gold nanoparticles, colorectal cells, pathology

Introduction

"There is plenty of room at the bottom" is the precious sentence from Richard Feynman initiating the field of nanotechnology.[1] Such a statement has turned into a complete field of new and exciting research which has since demonstrated that materials assembled at the nanometer scale possess unbelievable electrical, mechanical, and optical properties all based on the large surface area to volume ratios inherent in nanomaterials. Nanotechnology has brought widespread benefits to various fields of science, particularly in the biomedical sciences.[2–5] Nanostructures provide a wide range of applications in the areas of molecular imaging, early disease diagnosis, drug delivery, and tissue engineering to name a few due to their shape, size, surface charge, and functional groups.

In particular, the visible optical absorption and emission wavelengths of gold-based moieties make them appropriate candidates for photothermal therapy where light is

Correspondence: Behzad Nasseri; Thomas J Webster
Email bnaseri2000@gmail.com; th.webster@neu.edu

submit your manuscript | www.dovepress.com
DovePress
http://doi.org/10.2147/IJN.S248327

converted to heat to kill select cells, a property exciting specifically for anti-cancer applications. According to WHO statistics, annually, 8.9 million deaths result from all cancers representing the second highest cause of human death.[6–10] Plasmonic photothermal therapy, as a technique centered around a light-driven method, is considered as a novel paradigm shift in cancer treatment. The synergistic incorporation of photothermal therapy collateral with chemotherapy and radiotherapy promises sufficient increases in cancer treatment through PPTT.[11–14]

The mechanism of the destruction of the cancer cells by photothermal therapy has been realized by laser and nanostructural interactions when effective treatment occurs with appropriate nanoparticles. The heat created by nanoparticles depends on the laser and nanoparticle interactions via a localized surface plasmon resonance (LSPR) effect, which is a size- and shape-dependent property. In recent years, great interest has been seen in the therapeutic properties of different gold nanoplatforms towards LSPR. The impressive growth in the number of articles in this area illustrates the progress made in the fabrication and characterization of gold nanoparticles with specific morphologies categorized by their select optical properties from simple spherical structures stretching to more complex shapes.[15] The optical properties of noble metals, such as gold, are influenced by their size,[16–18] shape and surface modification of the nanostructure. The purpose of photothermal therapy includes the use of proper nanoparticles with extinction wavelengths in the near-infrared (NIR) region. Nanoparticles with their specific shapes could shift the resonance wavelength to NIR which is effective for the penetrating power of such wavelengths.

Gold nanorods with double extinction peaks have been introduced as appropriate morphologies with absorbing wavelengths around NIR. As a consequence, gold nanorods have been applied to deep tissues. The size of nanoparticles can be introduced as an additional factor to enable to shift from high absorbing wavelengths of visible ultraviolet (UV) toward NIR that are desirable for biomedical applications. In photothermal therapy, the red-shifting of the absorbing peak in nanoparticles is seen as impossible; however, the surface modification of gold nanostructures can help solve the problem.[19] Advances in the synthesis, modification and application of gold nanostructures in nanomedicine (such as PTT) have enabled such red-shifting of various shapes, such as rods,[20–22] shells,[23] cubes,[24,25] flowers[26] and dahlias[16] to name a few.

Because of their small dimension, simple functionalization and tunable optical properties, gold nanoparticles have been introduced as attractive nanostructures and have revolutionized biomedical applications[27] for improved medical imaging,[28,29] diagnosis,[30,31] treatment mechanisms[32] and drug delivery.[33] In photothermal therapy, more sophisticated shapes can be used such as prisms,[34] clusters,[35] matryoshka[36] and capsules.[37] The LSPR wavelength and cross-section in nanoparticles, which effect the therapeutic efficiency of photothermal therapy, are shape and size-dependent factors. Other factors that effect the LSPR environment include the dielectric coefficient, the capping agent used in synthesis, and the nanoparticle refractive index.

Gold nanostructures with sizes around ~10–200 nm are affected by applying appropriate laser irradiation through LSPR which coherently focuses the oscillation of band electrons in nanoparticles. The small size of nanoparticles also provides an opportunity for suitable functionalization and easy entrapping of administered nanostructures in the target region such as cancer cells and tissue. In anisotropic nanomaterials, such as gold nanorods, several different optical absorbing wavelengths, known as plasmon resonance bands, might be introduced.[38] The first peak is related to electron oscillation which is separated into the longitudinal (L) axis at a ~520 nm wavelength and the second transverse axis (T) is the width of the nanorods at a ~750 nm wavelength. By increasing the length to width ratio in nanorods, which is known as the "aspect ratio factor (AR)", the UV absorbance spectra increases and helps red-shift the LSPR (λmax) which should be strongly considered for laser selecting in PTT for clinical applications and in the terms of a treatment for deep cancerous tissue.[39,40] For gold nanospheres of different sizes, the LSPR (λ_{max}) alters from 520 nm to 900 nm as the unique absorbance peak correlates with the cross-section of the nanoparticles. In addition to the size and shape of the nanostructures, investigations have proved that nanoparticle surface modification and functionalization alter the surface chemistry of nanoparticles and photothermal therapy.[41]

For example, Huang and co-workers developed rattle-type metal nanotransducers for dual applications such as MRI-guided and photothermal therapy.[42] Also, investigations in the optical properties of nanomaterials demonstrated that the LSPR shifting of spherical gold nanoparticles can be achieved by surface decoration (functionalizing) with ultrafine noble metal nanoparticles (with and without interfacial lamination). Rattle-type magnetic core nanostructures (100 μL, 10 μg) demonstrated a 32°C to 46°C increment over 5 min during

in vivo experiments on HepG2 tumor-bearing mice. Gao et al also reported the use of multilayered gold nanoparticles (MLGSs) on MDA-MB-231 cells (a human breast adenocarcinoma cell line) and reported less than 10% living cells in the presence of photothermal therapy at 808 nm and 2 W for 5 min. These results demonstrated both low toxicity of nanomatryoshkas (with 90% cell viability and at a concentration of 50μg/mL) and a remarkable temperature rise (to about 58°C) through in vivo assessment by using 100 μL, 4 mg mL^{-1} of MLGSs.[36]

Another primary aperture used in the PPTT protocol for medical applications includes laser generation. The laser has a wide range of applications in therapeutic protocols and tumor imaging techniques, such as breast cancer imaging and therapy,[43] and also in typical applications in cosmetic domains with the earliest application of a laser in ophthalmology operations.[44] Photothermal tumor ablation is another category of therapeutic techniques in which a laser is used as external energy. Moderate laser types are proper for clinical use. However, the penetration depth of a laser beam into the tissue limits its therapeutic applications and optical tomography has tissue depth limitations.[45] Hence, an appropriate laser supplier has a severe impact on the therapeutic efficacy of ablative photodecomposition.

Many classifications of laser/tissue interactions are used in clinical procedures, eg thermal and photochemical interactions, plasma-induced ablation and also photo-ablation as well as photo-disruption. The penetration of a laser into the tissue and the stimulation of nanoparticles (via LSPR) can be strongly considered for plasmonic photothermal therapy. By choosing an appropriate laser (frequency) via PPTT and red-shifting of a laser's wavelength, the effective penetration depth of a laser can be improved.

Considering the above, the objective of this study was to develop a new gold nanoparticle for anti-cancer plasmonic photothermal therapy.

Experimental Section

Chemicals and Materials

Tetrachloroauric trihydrate ($HAuCl_4.3H_2O$), trisodium citrate ($Na_3C_6H_5O_7$) (99%), tetrakis (hydroxymethyl) phosphonium chloride (referred to hereafter as THPC), hexadecyl trimethylammonium bromide (CTAB, 98%), hydroxylamine hydrochloride ($HONH_2{\cdot}HCl$) (Sigma-Aldrich, USA), and dithiolated-polyethylene glycol (SH-PEG_{400}-SH) were provided by the Polymer Laboratory at Hacettepe University. Milli Q grade I distilled water was used for all solutions. All reagents were used as received without further purification.

Synthesis Procedures

The aqueous media synthesis of AuNPs used citrate sodium as a reduction agent for converting gold ions (Au^{3+}) to atomic gold (Au^0) through the Turkevich et al method.[46] The AuNRs were prepared through the double stages protocol which consists of gold seed formation and growth reactions via the Nikoobakht et al protocol.[47] The details of the synthesis have been provided in the supplementary data section(see the Gold nanoparticle (AuNPs) preparation and characterization section).

The PGNSs were synthesized by the attachment of the gold nanoparticles of various diameters together via dithiolated PEG_{400}(-SH-PEG_{400}-SH-) linker molecules.[48] The PEG-based molecules increased the biocompatibility of the nanoparticles as determined through cell culture assays.[49] Disulfide polyethylene glycol (HS-PEG_{400}-SH) was used for functionalizing LSAuNPs during PGNSs formation to form a target spot for the UFAuNPs for cell attachment (see the S6 section in the supplementary data section).[48,50]

The engineering of PGNSs for LSPR activation in the NIR region for this PPTT application was important. The detailed synthesis description of the PGNSs is given in the supplementary data section.

Characterization

The LSPR absorption of the nanoparticles were measured at 400 to 900-nm wavelengths by UV-vis spectrophotometry (JASCO, V-530). Transmission electron microscopy (TEM, JEOL JEM 1010, FEI, Tecnai) was used for measuring the size and crystallographic structure of the nanoparticles. Dynamic light scattering (DLS) of the synthesized nanoparticles were measured by a ζ-sizer (HAs 3000, MALVERN, USA). The characterization of the nanoparticles are reported in Table S1 and Figure S1 - Figure S4 section of the supplementary data section.

The nanostructures were characterized by a dynamic light scattering (DLS) (ζ-sizer) device to identify the size distribution and charge evaluation of the nanoparticles; see the Figure S1 section of the supplementary data section.

Numerical Modeling

COLMSOL multiphysics software was used for numerical modeling of plasmonic properties with proper initial and boundary conditions. Through modeling of the laser and nanoparticle interactions, we obtained the electrical intensity

(E_i) (details are given in the simulation model) which is proportional to an increase in temperature. Laser irradiation on different nanoparticles was modeled for theoretical (numerical modeling) investigations.

Cell Culture

A Duke's type Colorectal Adenocarcinoma malignant cell line (DLD-1; ATCC CCL-221 ™ originally purchased from ATCC) was provided as a gift from the Gulhane Training and Research Hospital, Turkey and a fibroblast cell line (ATCC CCL-1213 ™) was supplied from SAP Institute (Turkey). The cells were seeded at 1×10^4 cells/well. RPMI-1640 media, 10% fetal bovine serum (FBS) and penicillin and gentamicin were provided from the Bioengineering Department of Kirikkale University (Turkey). Cells were incubated in a 95% O_2 and 37°C humidified environment for 24 hrs. The cells were detached from the flask by using trypsin-ethylene diamine tetraacetic acid (EDTA) after proper proliferation to obtain a sufficient number of cells (confluency of 85%).

Photothermal Assays on Nanoparticle Dispersions

To evaluate the temperature increase from the nanoparticles (PGNSs, AuNPs and AuNRs), aqueous (2 mL) dispersions with a 300 µg/mL (1.03×10^{13} NPs/mL) concentration were irradiated using a 534 nm, 606 nm and 808 nm (NIR) laser (450 mW output) at a laser intensity of 4 W/cm^2 for 5 min. The distance between the upper level of the solution and the laser was adjusted to 3 cm. Temperature enhancement images were obtained by capturing the images given using an IR thermal camera (FLIR, i5, Germany). The results of the temperature rising through the different intervals showed the photostability of the synthesized nanoparticles which was accomplished by completing several measurements of extinction spectra of the nanoparticles before and after the laser irradiation and using UV-vis spectrophotometer data. The photostability of the nanoparticles is highly important during photothermal therapy.

MTT Assays

The in vitro cytotoxicity effect of the synthesized PGNSs was evaluated on the DLD-1 and fibroblast cells using a standard MTT assay. For this, wells were seeded with cells in 12 cavity well-plates at a density of 10^4 cells/well in RPMI-1640 medium at 5% CO_2 for 24 hrs. The relative cell viability indexed was evaluated using MTT experiments. The protocol used is given in the supplementary data section.

Photothermal Ablation of the DLD-1 and Fibroblast Cells in vitro

The DLD-1 cells and fibroblast cells were cultured in 12 well plates in the presence of RPMI-1640 medium complemented with 10% FBS for 24 h at 37°C and 95% O_2 humidified conditions. For this, the cells were incubated with the highest non-toxic concentration of PGNSs (300 µg/mL equals $1.03\times10^{13} NPs/mL$) achieved from the MTT assays for an additional 4 h. Afterward, the excessive amount of medium and PBS for washing the cells was decanted. The cells were irradiated by a proper laser (808-nm, 4 W/cm^2 for PGNSs) for 5 min. Negative control groups (no laser irradiation and no nanoparticles) were selected for appropriately analyzing the results. To study the effect of different power intensities on the photothermal ablation of DLD-1 and fibroblast cells, an aliquot of 200 µL of PGNSs, AuNRs and AuNPs (300µg/mL, 200µg/mL and 100µg/mL) in RPMI-1640 was incubated with the cells for 5 hrs at 37°C and 95% O_2. Thereupon, the cells were irradiated to 808-nm, 606-nm and 532-nm

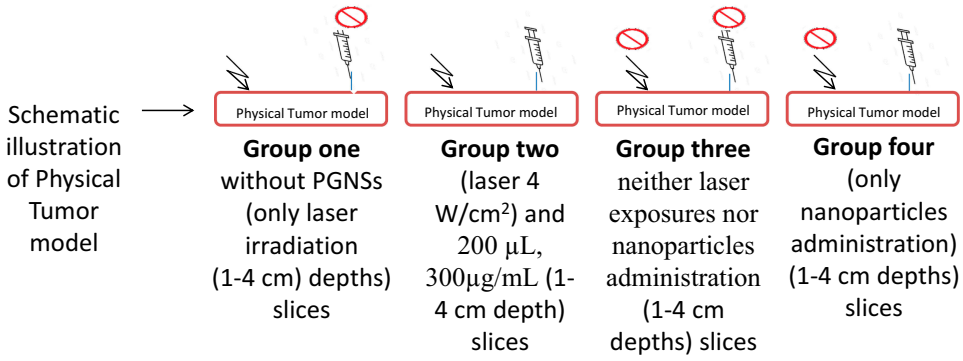

Figure 1 Photothermal therapy in the physical tumor model showing the different groups used.

laser with different powers (1, 3 and 4 W/cm^2) for 5 min and placed at 37°C for a further 1 hr. All measurements were conducted in quadruplicate.

Physical Model of PPTT

A non-living physical tumor model was used for the evaluation of how much of the PPTT penetrated into the tissue and what can be imagined to assess tissue structural changes after use (Figure 1). The slices of the model were studied through negative and positive control groups (n=3). One group was exposed to a laser alone (without PGNSs present) and the second group was exposed by a laser after PGNS (200 µL, 300µg/mL) injection. The third group neither was exposed to the laser nor were the nanoparticles administered and for the fourth group, only nanoparticles were administered.

Statistical Analysis

All of the statistical analyses related to the MTT assays and other experiments were performed by one-way analysis of variance (ANOVA) followed by OriginPro 9.1 software compatible tests of the Bonferroni post hoc method. In addition, all data are represented as the mean ± SD of at least n=3 independent sets of experiments.

Results and Discussion

Characterization of PGNSs

To synthesize the PGNSs nanocomposites, the decoration of the core nanoparticles (LSAuNPs) with ultrafine gold nanoparticles (UFAuNPs) was completed. Transmission electron microscope images were used to observe the morphology, crystallography and shape of the nanoparticles (Figure 2A). UV-vis absorption spectra (Figure 2B) illustrated that the LSPR wavelength of the UFAuNPs was centered at 502 nm and the size distribution (Figure 2C) of the monodispersed gold seeds presented as the as-prepared gold seeds were 2–5 nm in diameter revealing sufficient data for the formation of gold nanoparticles by ionic gold (Au$^+$) reduction. Figure 2 gives information

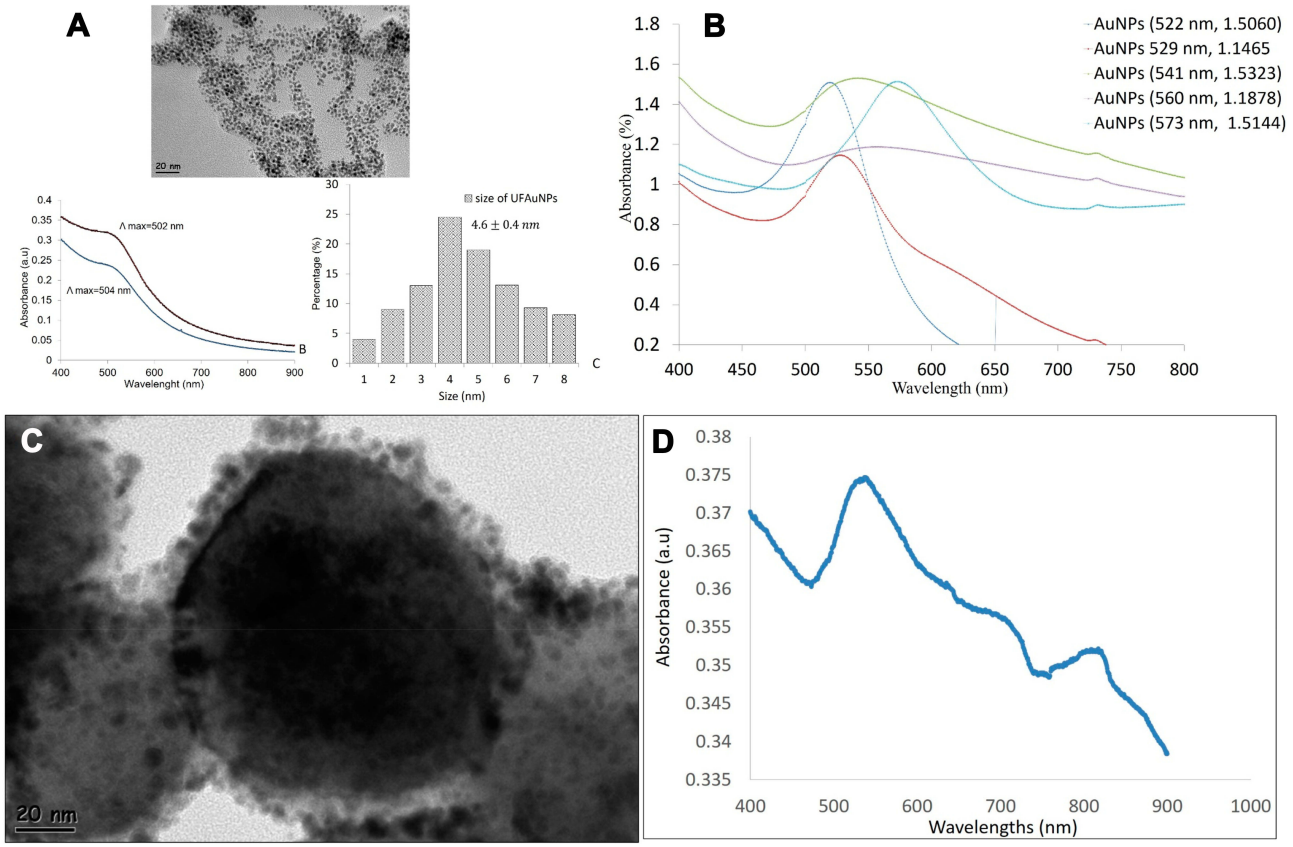

Figure 2 Characterization of the nanoparticles, (**A**, above) high-resolution transmission electron micsocope (HRTEM) image (FEI, Tecnai, 280kv), (**A**, left) absorption spectra of gold seeds centered at 505 nm, (**A**, right) size distribution diagram of the gold seeds, (**B**) UV-Vis spectrum of the gold core nanoparticle growth, (**C**) crystallography image of PGNSs acquired by HRTEM presents gold seed (UFAuNPs) decoration on the core gold nanoparticles with an absorbing peak wavelength by (**D**) UV-Vis spectroscopy.

about the monodispersed formation of UFAuNPs without agglomeration. The PGNS core is shown as the large gold core nanoparticle (LSAuNPs) as given in Figure 2 (bottom). The extinction wavelength (Figure 2 (above/right)) resulting from the UV-vis spectrophotometer illustrates the growth stages of the bare gold core. HRTEM images (Figure 2, bottom/left) (Figure S7) of the PGNSs reveal the shape and crystallography of the PGNSs showing nanoparticles around 80 nm in diameter. Figure 2 (bottom/right) shows the UV-vis spectrum of the PGNSs in the ultraviolet-visible region. PGNSs activation at the 784 nm wavelength provides evidence of the ability of the nanoparticles to serve in photothermal medical applications.

Modeling of the Heat Generation During Plasmonic Photothermal Therapy and Plasmon–Plasmon Interactions in Different Nanostructures by COMSOL

In this section, a COMSOL multiphysics program was used for numerical simulation of the plasmonic photothermal therapy. The electrical intensity caused by the nanostructures

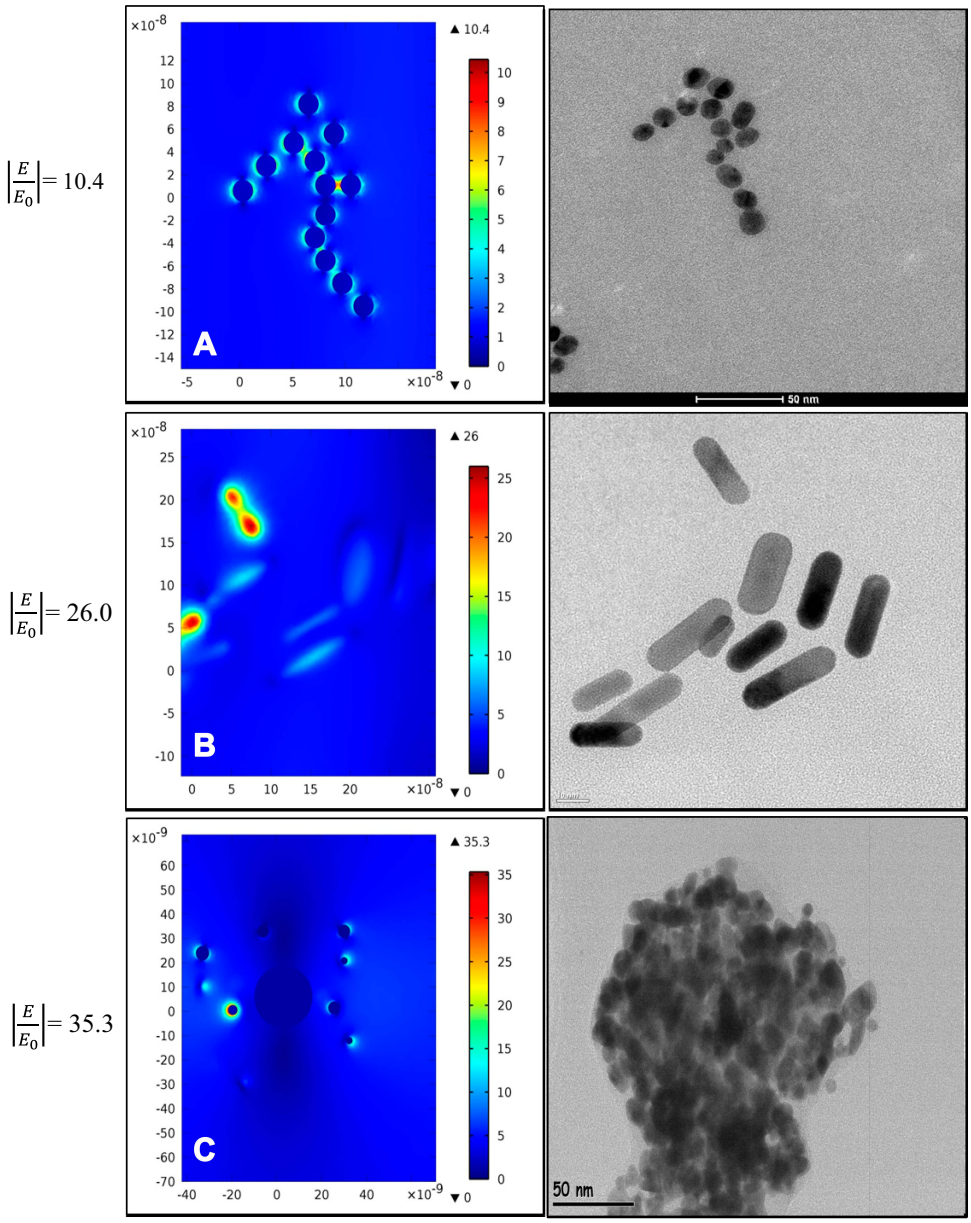

Figure 3 The predicted numerical modeling of electrical field intensity in terms of laser induced nanoparticles, normalized to the incident field of AuNPs (top), AuNRs (middle) and PGNSs (bottom) (COMSOL multiphysics).

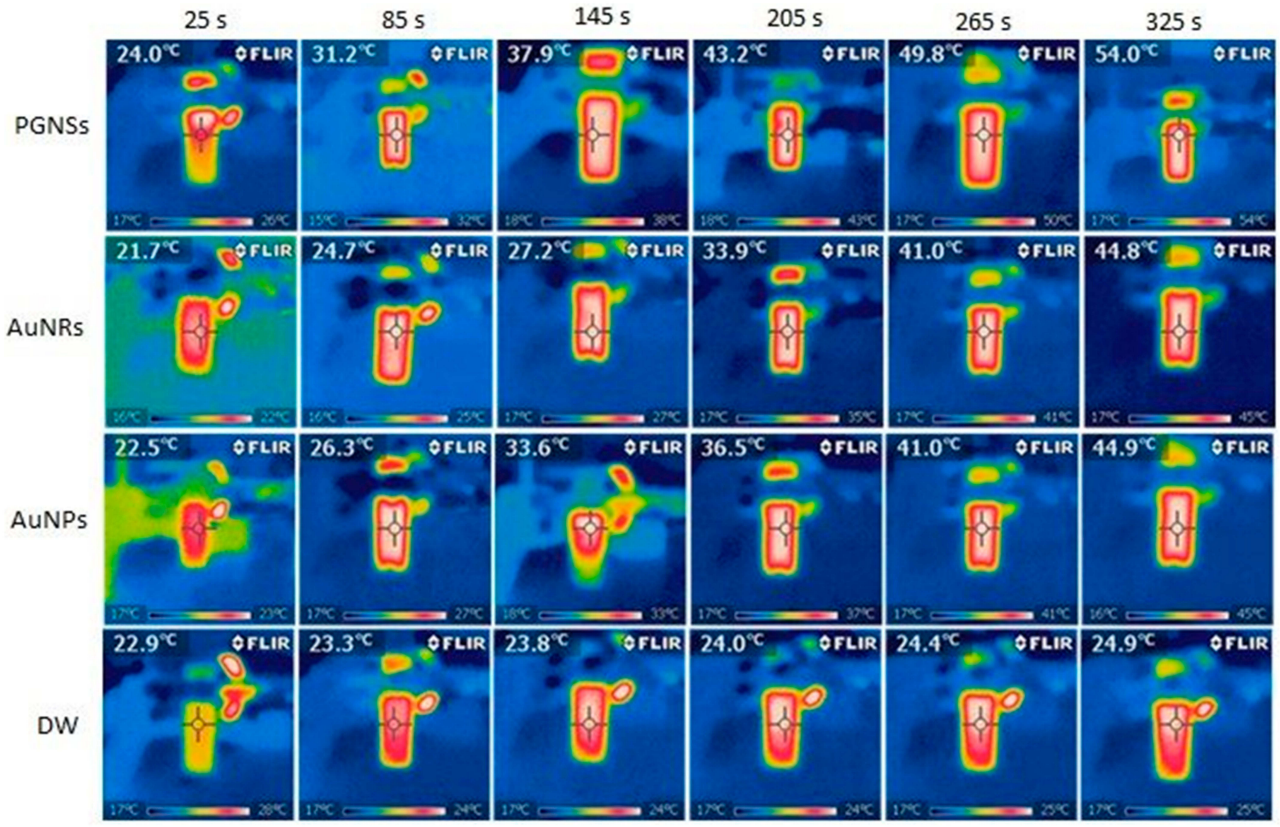

Figure 4 The real-time photothermal heating of laser exposed PGNSs, AuNRs and AuNPs at 300 μg/mL captured by an infrared thermal camera (FLIR i5).

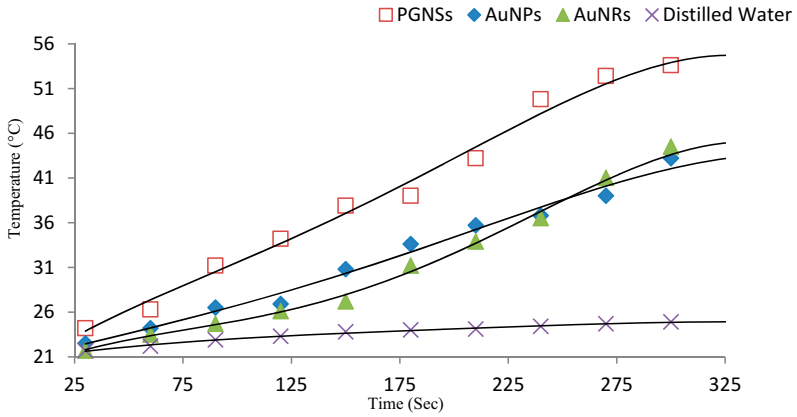

Figure 5 Temperature plots of the nanostructured dispersions (1.03×10^{13} NPs/mL) exposed to a diode laser ($4W/cm^2$).

and laser interaction was stimulated in this section. The plasmonic modeling of PGNSs, AuNRs and AuNPs were done according to the HRTEM images of the nanostructures which were previously shown in Figure 3. The image in Figure 3 reveals the electrical field enhancement of the nanoparticles which resulted from the local surface plasmon resonance (LSPR) ($|E|$). The partial converting of the electrical field appears in the form of heat in the PPTT. The results gave information for the $\frac{|E|}{|E_0|}$ ratio and in the case of AuNPs (Figure 2, top), the ratio of 10.4 in comparison to 26.0 and 35.3 for AuNRs and PGNSs, respectively (Figure 3, middle and bottom). According to the $\frac{|E|}{|E_0|}$ ratio, in the case of different nanoparticles, the PGNSs allocated the highest

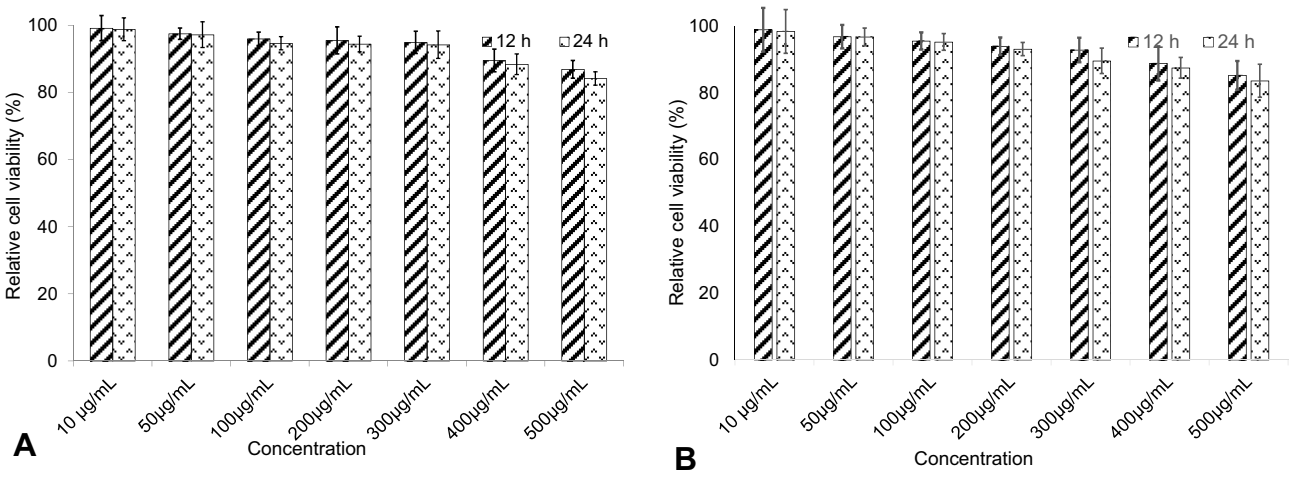

Figure 6 The cytotoxic effects of the nanoparticles after 12 h and 24 h; (**A**) fibroblast cells and (**B**) DLD-1 cells (n=3).

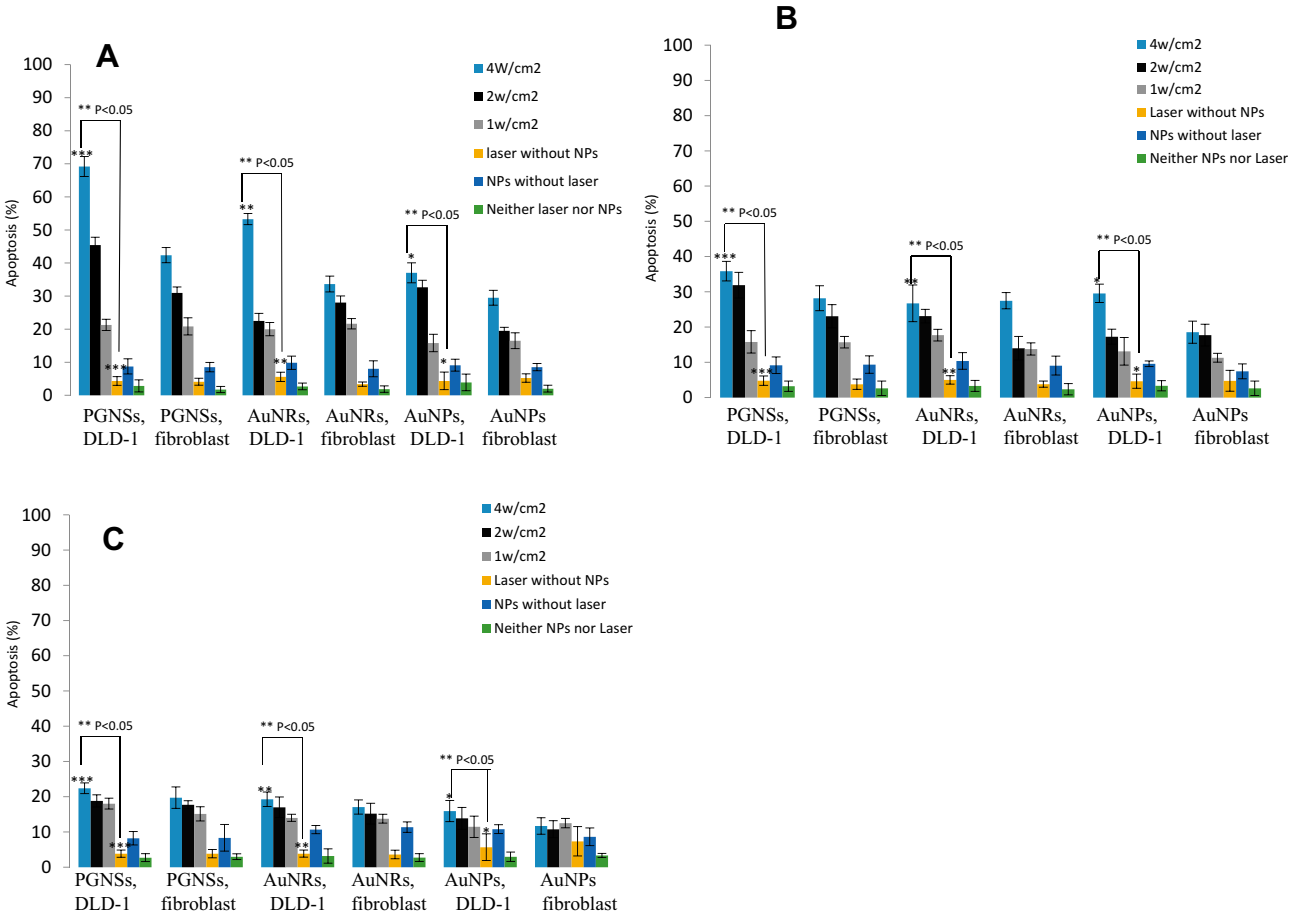

Figure 7 Apoptosis indexes of DLD-1 and fibroblasts cells due to the PPTT mechanism. Different nanostructures were exposed to 808 nm, 650 nm and 532 nm lasers at 4, 2 and 1 W/cm^2 power for; (**A**) 1.03×10^{13} NPs/mL, (**B**) 0.89 ×10^{12} and (**C**) 2.5×10^{11} AuNPs/mL concentrations ($p < 0.05$). Data are presented as mean SD from three independent experiments. *, ** and *** indicares the apoptosis values differences between PGNSs, AuNRs and AuNPs and laser without nanoparticles.

$\frac{|E|}{|E_0|}$ ratio meaning the maximum light-to-heat conversion rate in comparison to the laser-exposed nanoparticles (AuNRs and AuNPs). The highest ratio of E was caused by near field interactions of the localized plasmon–plasmon effect of gold dots on the surface of the core part and core nanoparticles.

Heat Produced by Laser Irradiated Nanoparticles Through Plasmonic Photothermal Mechanisms

To further investigate the light-to-heat conversion for the plasmonic photothermal mechanism, the samples were prepared by laser charging 2 mL of 1.03×10^{13} NPs/mL from each PGNSs, AuNRs and AuNPs nanostructure formulation in an Eppendorf tube and recording the real-time values. The laser power and exposure times are critic factors in plasmonic photothermal therapy. The results are presented as thermography images (Figure 4) captured by an IR thermal camera (FLIR, FLIR Systems i5, Boston, MA, USA). Laser-nanoparticle incidence was realized by using a laser at 808-nm and $4W/cm^2$. The laser-nanoparticle incidence was recorded at 60 s each.

The temperature gradient (Figure 5) describes the time-dependent temperature ($T_{act.}$) values between the lasers exposed to the nanoparticles and the ambient temperature (T_{amb}). In Figure 5, ΔT_{PGNSs}=29.8°C by applying a laser (808 nm, $4W/cm^2$) at the end of 325 s when the values were ΔT_{AuNRs} =23.1°C and ΔT_{AuNPs} =21°C. A negligible rise in temperature was seen regarding distilled water (ΔT_{DW}=3.2°C) with the same laser power and exposure time.

The lowering temperature at the end of the irradiation time shows the probable agglomeration and reduction in nanoparticle photostability. The COMSOL modeling (electrical field enhancement) in terms of PGNSs, AuNRs and AuNPs (Figure 4) confers the temperature gradient results from the nanoparticle dispersions (Figure 5).

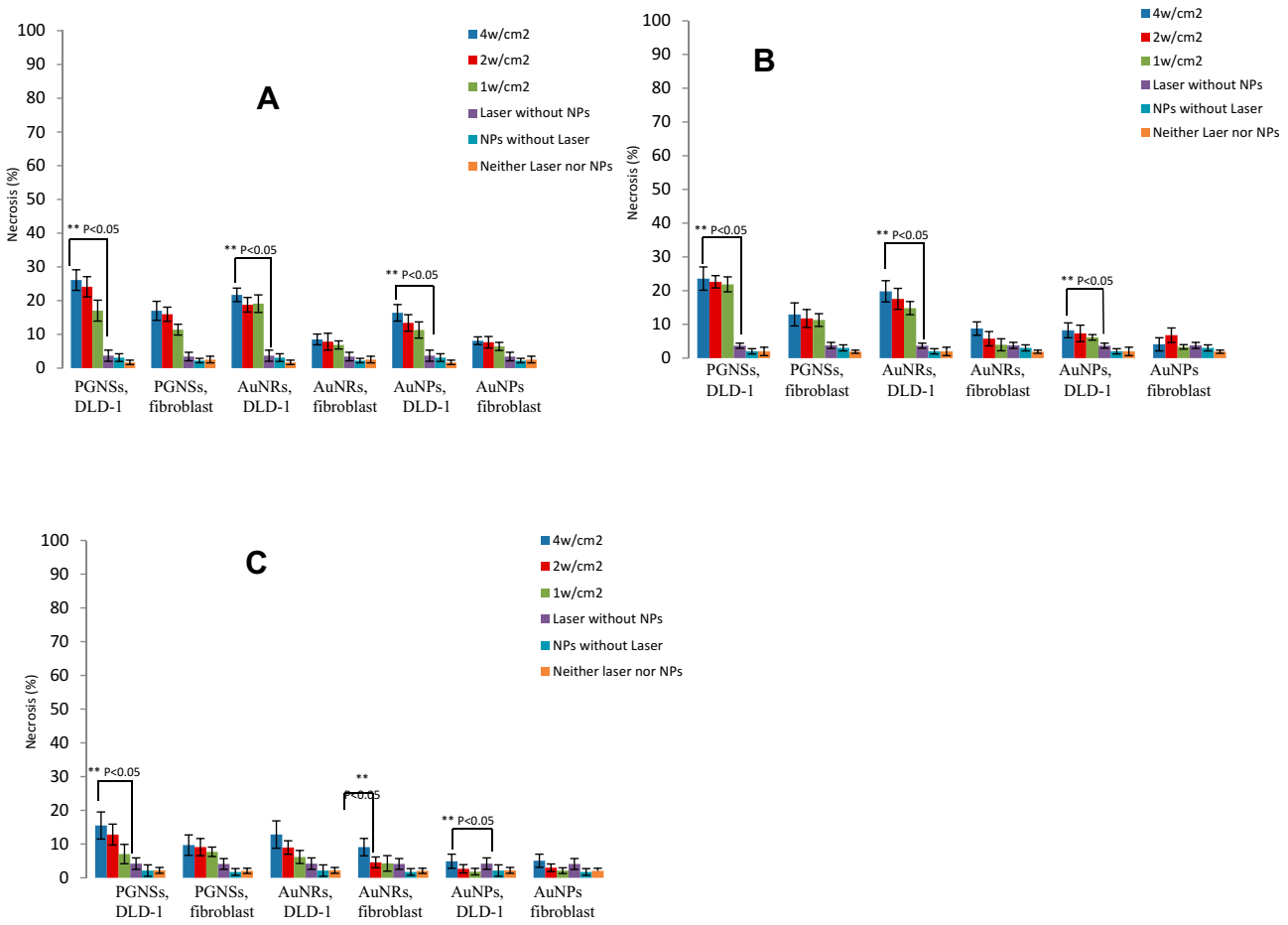

Figure 8 Necrosis indexes of DLD-1 and fibroblast ells due to the photothermal heat at (**A**) 1.03×10^{13} NPs/mL, (**B**) 0.89×10^{12} and (**C**) 2.5×10^{11} AuNPs/mL concentrations (** $p < 0.05$). Data are presented as mean SD from three independent experiments.

In vitro Cytotoxicity of PGNSs

Before applying the photothermal mechanism on the cells, it was necessary to evaluate the cytotoxicity effects (relative cell viability %) of the PGNSs on DLD-1 cell and fibroblast cell lines according to standard MTT measurements. The assessment was completed after 12 h and 24 h of cell incubation at different concentrations of PGNSs. Cell viability results (Table S4 and Figure 6) show acceptable values of viability as can be seen even after 24 hrs in 300µg/mL of PGNS incubation where the DLD-1 (89.4%) and fibroblast cells conserved their high viability (above 94.2% of live cells). The lower cytotoxic effect of PGNSs demonstrates initial promise for nanomedicine applications. The 300 µg/mL concentration can be considered as the toxicity limit for the biological assays of this study.

Photothermal Therapy Effects on Cells

The DLD-1 and fibroblast cell lines were monitored for apoptotic and necrotic cell death during PPTT as illustrated in Figures 7 and 8. Figure 7 demonstrates that apoptosis occurred for the DLD-1 cells by applying PGNSs with AuNRs and AuNPs at a 1.03×10^{13} NPs/mL (300 µg/mL) concentration. Figure 7A reports apoptosis values when using a 4 W/cm^2 laser and 1.03×10^{13} NPs/mL. The PGNSs resulted in the highest apoptosis for the DLD-1 cells (at 68.75% of cells undergoing apoptosis) whereas 45.67% and 30.88% were reported for the case of 2 and 1W/cm^2 laser powers, respectively. The results highlight the proportional of laser power to apoptotic cells.

For the fibroblast cells, and at similar conditions of laser power (4 W/cm^2) and nanoparticle concentration (1.03×10^{13} NPs/mL), the highest apoptosis value (at 41.33%) was reported for the PGNSs group, whereas 30.88% and 19.72% were reported for the case of 2 and 1 W/cm^2 laser powers, respectively. The collective results showed that the DLD-1 cells were much more sensitive to photothermal heat generation than fibroblasts.

Further, to investigate the relationship between apoptosis and nanoparticle concentration, the PGNSs were incubated with cells at different concentrations at a constant

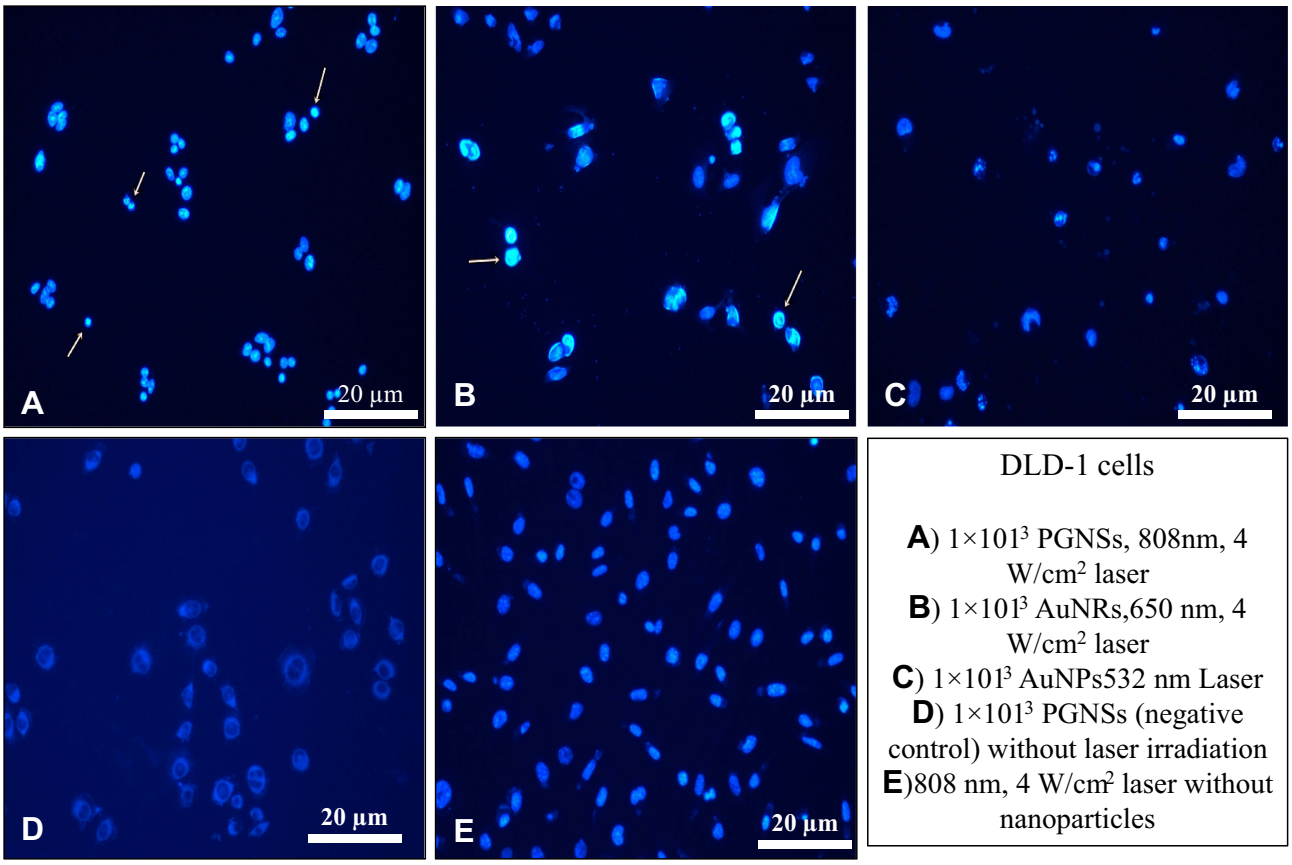

Figure 9 Representative fluorescent microscope images of the apoptotic DLD-1 at (**A**) PGNSs incubated with laser (808 nm and 4W/cm^2), (**B**) AuNRs incubated with laser (650 nm and 4W/cm^2), (**C**) AuNPs incubated with lased (532 nm and 4W/cm^2), (**D**) PGNSs inubation without laser exposure, and (**E**) laser irradiation alone (808 nm and 4W/cm^2) without nanoparticles. White arrows present the structural lysis like changes in the cells which are marked for apoptotic cells that are shinny.

power of laser irradiation. For the PGNSs group in Figure 7A–C, the results showed 68.75%, 36.58% and 21.12% apoptosis when using laser exposures (4 W/cm^2) at 1.03×10^{13}, 1.03×10^{12} and 1.03×10^{11} NPs/mL concentrations, respectively. The comparison between apoptosis caused by PPTT from the PGNSs and AuNPs groups highlighted a mildly more lethal effect of AuNPs on DLD-1 cells than PGNSs. For the 4 W/cm^2 laser power, 37.54%, 26.32% and 15.78% (Figure 6A–C) of cells underwent apoptosis when exposed to 1.03×10^{13}, 0.89×10^{12} and 2.5×10^{11} AuNPs/mL concentrations, respectively, which shows a sensible reduction in apoptosis compared to the PGNS group. In Figure 7A and for the 1, 3 and 5 series, 68.75%, 52.66% and 37.54% were reported at the 1.03×10^{13} NPs/mL concentration of PGNSs, AuNRs and AuNPs irradiated by a 4W/cm^2 laser, respectively.

Collectively, the apoptotic DLD-1 cell results (Figure 7) demonstrate the most effective photothermolysis (cell killing) for the pimpled gold nanoparticle group which demonstrated efficient conversion of light to heat for the PGNSs via PPTT compared to AuNRs and AuNPs.

Necrosis Results for DLD-1 and Fibroblasts Exposed to Photothermal Therapy

The in vitro toxic photothermal effects of PGNSs, AuNRs and AuNPs were studied using DLD-1 cells and fibroblast cells. The results of necrosis (Figure 8) and also that in the supplementary data (Tables S1–S10) revealed the lethality of the cells to the present treatments via a necrotic mechanism. Specifically, Figure 8A–C shows cell death caused by the different nanoparticles at the 1.03×10^{13} NPs/mL (300 µg/mL), 0.89×10^{12} NPs/mL (200µg/mL) and 2.5×10^{11} NPs/mL (100 µg/mL) concentrations, respectively. According to the graphs in Figure 8A, 26.21, 24.3 and 16.49% (necrosis indexes) for the PGNSs, AuNRs and AuNPs (300 µg/mL) at different laser powers (4, 2 and 1 W/cm^2) are reported, respectively. Minor differences in the results demonstrated that necrosis was low due to the laser

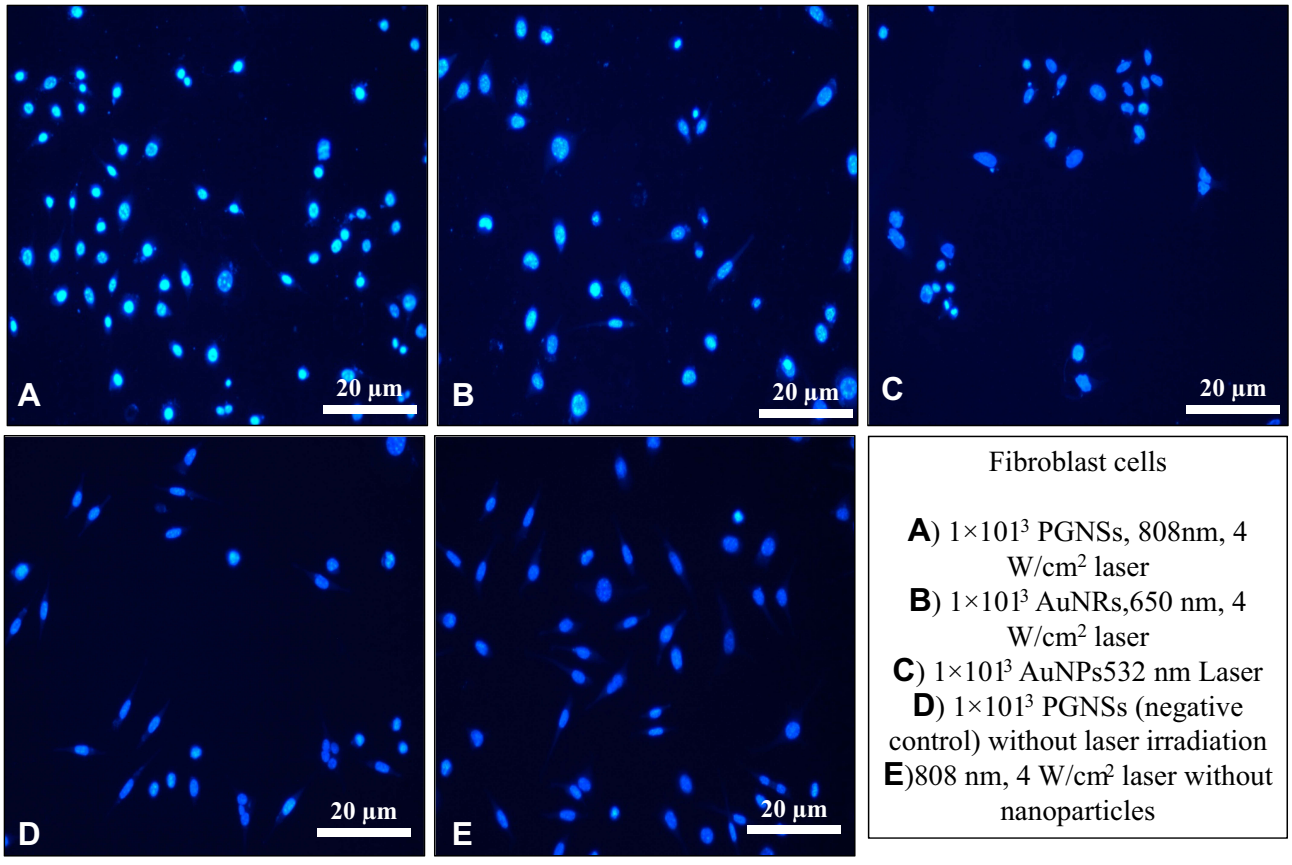

Figure 10 Representative fluorescence microscope images of the apoptotic fibroblast cells at (**A**) PGNSs and laser (808 nm and 4W/cm^2), (**B**) AuNRs and laser (650 nm and 4W/cm^2), (**C**) AuNPs and lased (532 nm and 4W/cm^2), (**D**) PGNSs incubation without laser exposure, and (**E**) laser irradiation alone (808 nm and 4W/cm^2) without nanoparticles.

power. For the PGNS group, DLD-1 cell death due to necrosis for the 1.03×10^{13}, 0.89×10^{12} and 2.5×10^{11} NPs/mL concentrations were 26.21%, 22.4% and 14.76%, respectively, which showed a minor correlation of nanoparticle concentration to necrosis.

The photothermal studies revealed the greatest ability of the PGNSs to lyse cancer cells compared to AuNRs and AuNPs with 26.21%, 21.22% and 16.32% necrosis at the 300 µg/mL concentration and 4 W/cm^2 laser power, respectively. Also, it was observed that necrosis and laser power have direct correlations wherein at 4, 2 and 1 W/cm^2 laser powers, the PGNSs showed 16.6%, 15.76% and 11.4% necrosis, respectively. Figure 8A further provides information concerning the higher sensitivity of the DLD-1 cells to the toxic photothermal heat generated than fibroblast cells according to the necrotic cell death indexes. Also, the PGNSs (300 µg/mL) had the highest necrosis index (16.6%) compared to the AuNRs and AuNPs groups which were at 12.2% and 9.4%, respectively. The difference of necrotic cell death at lower nanoparticle (100µg/mL) concentrations for the PGNSs, AuNRs and AuNPs groups were less (8.5%, 4.18% and 2.8%, respectively) which highlight the lower necrosis effect of photothermal heat at low concentrations of nanoparticles.

Apoptosis in DLD-1 and Fibroblast Cells in Fluorescence Microscope Images

In vitro PPTT experiments and the cell lethality caused by toxic heat were also observed via fluorescent microscopic images. Propodium iodide staining was used to provide information about DLD-1 cells dying via the apoptosis mechanism (Figure 9A–E). As stated, apoptosis was correlated to laser power and nanoparticle concentration. In Figure 9A, the highest apoptosis occurred for the PGNSs group while mild apoptosis was shown for the AuNRs and AuNPs (Figure 9B and C). Figure 9D shows the apoptotic DLD-1 cells for the

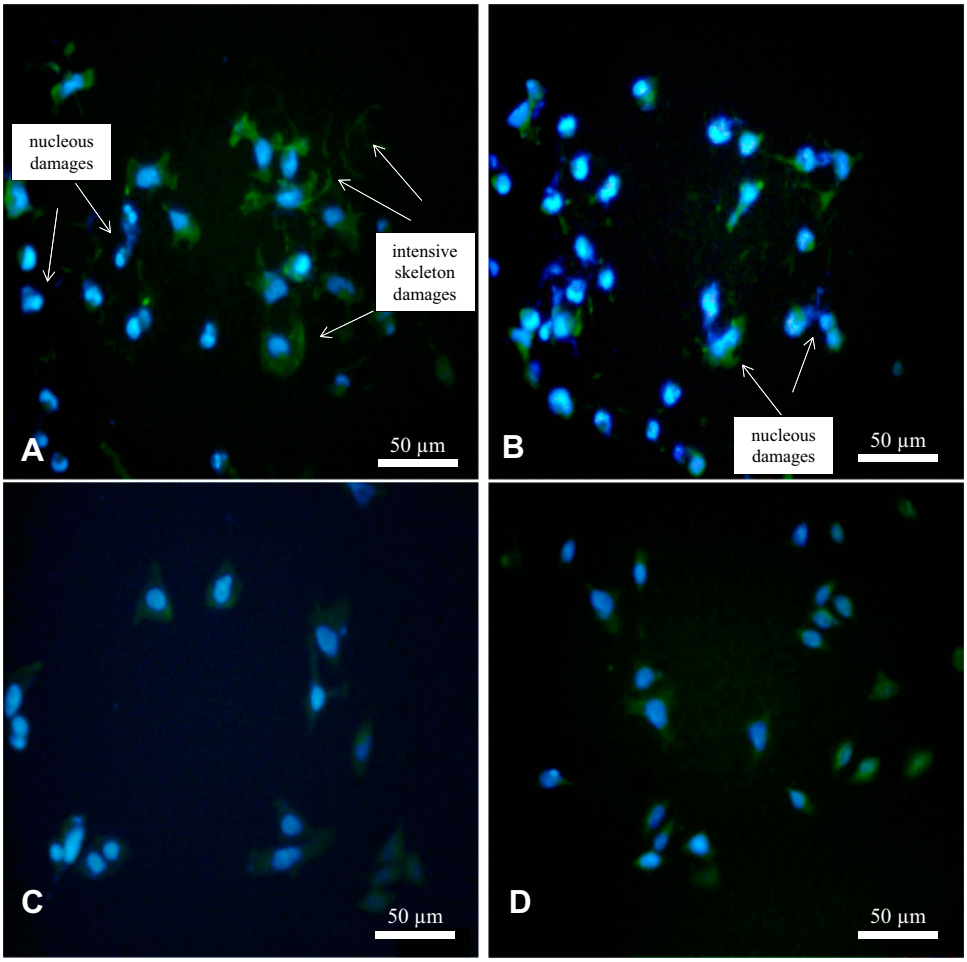

Figure 11 Fluorescence microscope images of DLD-1 cells treated with different nanoparticles for (**A**) PGNSs, (**B**) AuNRs, (**C**) AuNPs and (**D**) without nanoparticles incubation in the negative control group.

PGNSs at its highest concentration (300 µg/mL) without laser irradiation and Figure 9E shows the apoptotic cells exposed to an 808-nm laser beam alone (without nanoparticles) (negative control group). As seen in Figure 9D and E, negligible apoptosis was detected which provides evidence of the low hazardous effect of the laser alone and nanoparticle exposure.

Also, Figure 10A–E shows the apoptotic fibroblast cells results through PPTT. As shown in Figure 10A, PGNSs were highly effective for killing cells via the plasmonic photothermal therapy mechanism (with more bright spots showing apoptosis in cells) compared to the AuNRs and AuNPs with an obvious lower apoptosis index (lower amount of bright spots).

Figure 10A–C shows fluorescent microscopy images of apoptotic fibroblast cells treated with PGNSs, AuNRs and AuNPs. Figure 10D shows the apoptosis of fibroblast cells without laser exposure and Figure 10E shows the apoptotic photothermal ablation in fibroblast cells under laser exposure alone (negative control group). The high apoptosis indexes for the DLD-1 cells identified the high sensitivity of DLD-1 cells against the toxic heat of PPTT generated by PGNSs compared to fibroblast cells (the values in Figures 7, 9 and 10). This can be explained since the highest cell lethality occurred for the PGNSs group (Figure 10A) followed by AuNRs (Figure 10B) and AuNPs (Figure 10C). Additional data concerning apoptosis and necrosis of DLD-1 cells at various nanoparticle concentrations are included in the supplementary data section (Figure S5).

The simultaneous staining of cells revealed detailed information about the structural damage in the cells PPTT exposure. Fluorescent microscope images of DLD-1 cells (Figure 11) showed severe heat damage towards F-actin filaments in the cytoskeleton during PPTT.

The obvious destructive effects of PGNSs can also be seen in Figure 11A. The remarkable nucleus and cellular skeleton disintegration (serious irreversible damage) during PPTT heat can be clearly seen. Sensible changes, such as fading (karyolitic), shrinkage (pyknosis) and

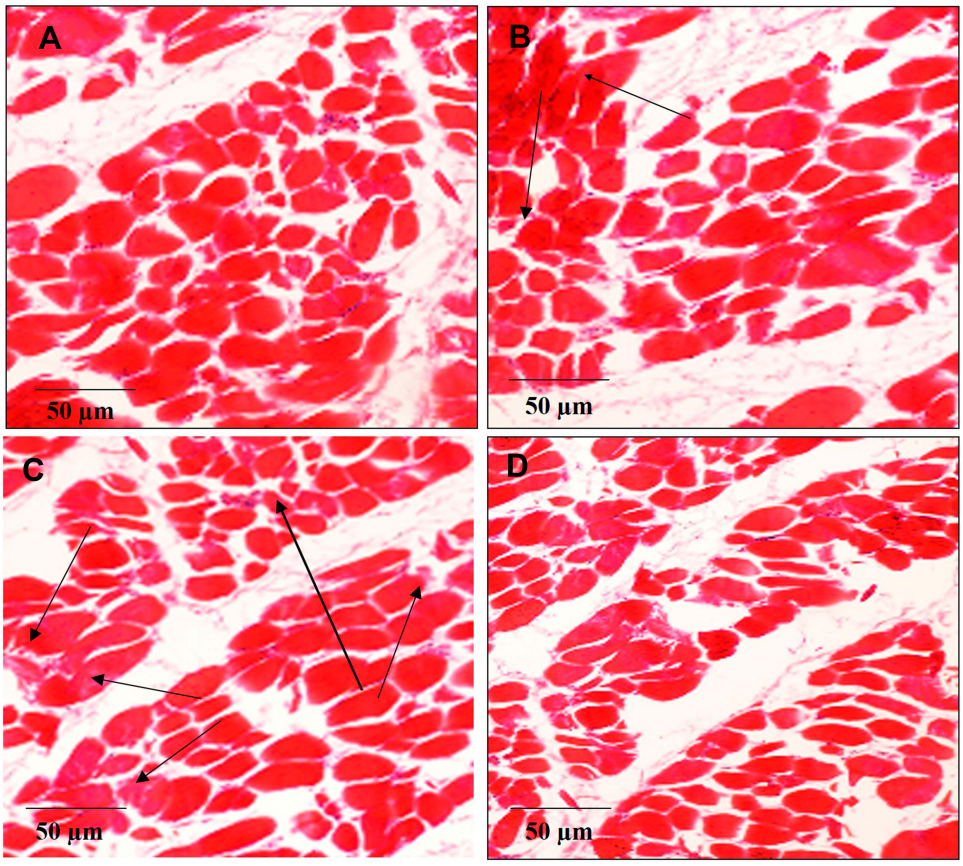

Figure 12 Tissue morphology changes by PPTT and pathology observations in hematoxilin and eosin (H&E) stained chicken breast at different tissue penetration depths for the (**A**) negative control group without nanoparticle treatment (total depth of speciment), (**B**) PGNSs treated tissue in a 100 µm thickness slice (532 nm laser with the same power mentioned above), (**C**) a 200 µm thickness inside the tissue, and (**D**) thickness of 900 µm inside the tissue (scale bar 50 µm). The black arrows (**B**) describe the degenerative changes in the structure of tissue, that used the PGNSs in the PPTT, and the black arrows (**C**) shows a rear side image of the tissue which represent no significant structural damage.

karyorrhexis, in the nucleus and also swelling and fragmentation between the skeleton and nucleolus are shown which are common effects due to toxic heat are during PPTT (Figure 11). In Figure 11B in terms of the AuNR group, the cell compartments experienced less degeneration (irreversible changes) than for the PGNS group. Photothermal therapy induces different types of cell damage including low damage levels (reversible) stretching to serious injuries (irreversible). Here, the AuNPs created reversible heat damage (Figure 11C) whereas the PGNSs produced remarkable cell lysis (Figure 11A). Figure 11D shows the changes in the negative control group with laser alone exposure without nanoparticles where considerable changes in both the cellular skeleton and nucleus were not observed. This illustrates the lack of cell damage when the laser is used alone in photothermal therapy.

Chicken Breast as a 3D Model for Laser Penetration

In this section, the laser–tissue interactions (nanoparticles with the laser energy) were determined to see the injury and structural changes in tissue caused via PPTT. The PGNSs (300 µg/mL, 200 µL) were inserted ex vivo into chicken breast tissue (a 3D physical model) (Figure 12). A laser beam was then applied to the target point. In the next step, pathology staining was completed in order to determine the most efficient laser penetration depth using the PPTT technique.

Figure 12A shows the structural changes in tissue created by laser beam exposure without nanoparticle administration. In Figure 12A and in the laser/tissue pinpoint tissue, minimal damage was observed for the laser without nanoparticles even at full tissue depth (penetration to 1.2 mm). For the microscopic observations in Figure 12B, serious damage to the

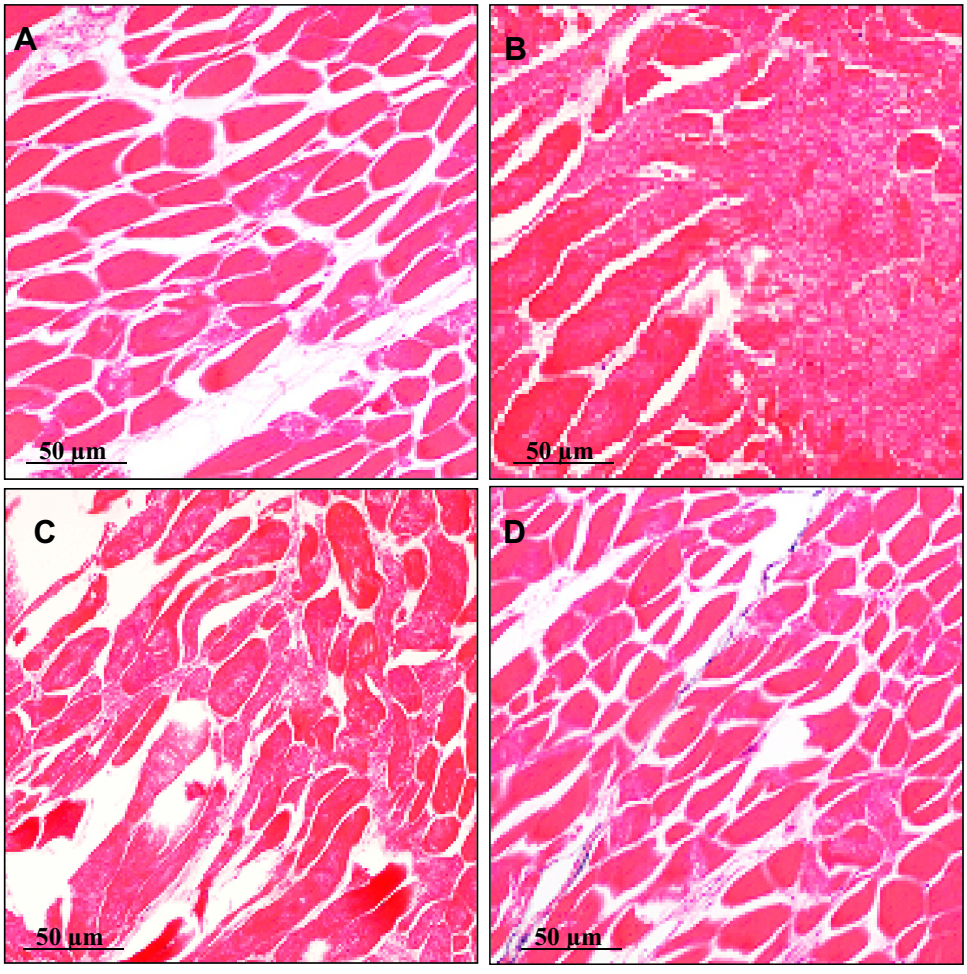

Figure 13 Chicken breast tissue (3D phantom) as a model to study the structural changes in laser/nanoparticle interactions per effective penetration depth in the (**A**) negative control group with laser exposure and without nanoparticles at a (**B**) depth of 0.6 cm, (**C**) 2.0 cm and (**D**) 3.0 cm in the tissue.

tissue slice (100 µm depth) could be seen in the region of the laser/nanoparticle (PGNSs) interaction. At depths of 200 µm inside the tissue (Figure 12C), no changes occurred due to PPTT, and in Figure 12D, no obvious structural changes in the rear side of the tissue at a depth of 500 µm with laser were observed. According to Figure 12, in spite of the high energy of the 532 nm laser (due to the restricted light penetrating power of the 532 nm wavelength), negligible heat damage appeared up to 100 µm. So, for the PGNSs treated condition, its penetration depth was limited by hundreds of micrometers inside the tissue.

The pathological observations given in Figure 13 reveal the structural changes of the tissue in the laser-exposed (808-nm, 4W/cm^2) PGNSs region. Figure 13A shows the negative control group in the chicken breast tissue irradiated by the laser alone (without nanoparticle administration) at a depth of 5 mm. The microscopic image demonstrates no remarkable changes in the tissue by the NIR laser (808-nm).

In Figure 13B, the breast tissue was sectioned by 0.6 cm slices and exposed to a laser in the presence of PGNSs. As seen in Figure 13B, mild degenerative changes occurred in the muscle filaments and thermal effects were seen. The structural changes in Figure 13C were less than the pathology observations (at the depth of 2.0 cm). Figure 13D relates to the pathological observations at 3.0 cm depths via PGNSs/laser interaction. As seen in image 13C and D, and in spite of the higher penetration depth of the 808-nm laser (and its much lower energy compared to the 532-nm laser), no remarkable damage per greater tissue depth was observed. Finally, the pathological observations confirmed no irreversible damage to the tissue (Figure 13A, C and D) but, conversely, irreversible muscle filament defects could be seen due to photothermal damage (Figure 13B).

Photothermal Effects on Non-Living Physical Model of Liver Tumors

In this section, the potentially damaging effect of PPTT (laser exposed PGNSs) was studied. Structural changes using a tumor tissue model were observed besides further

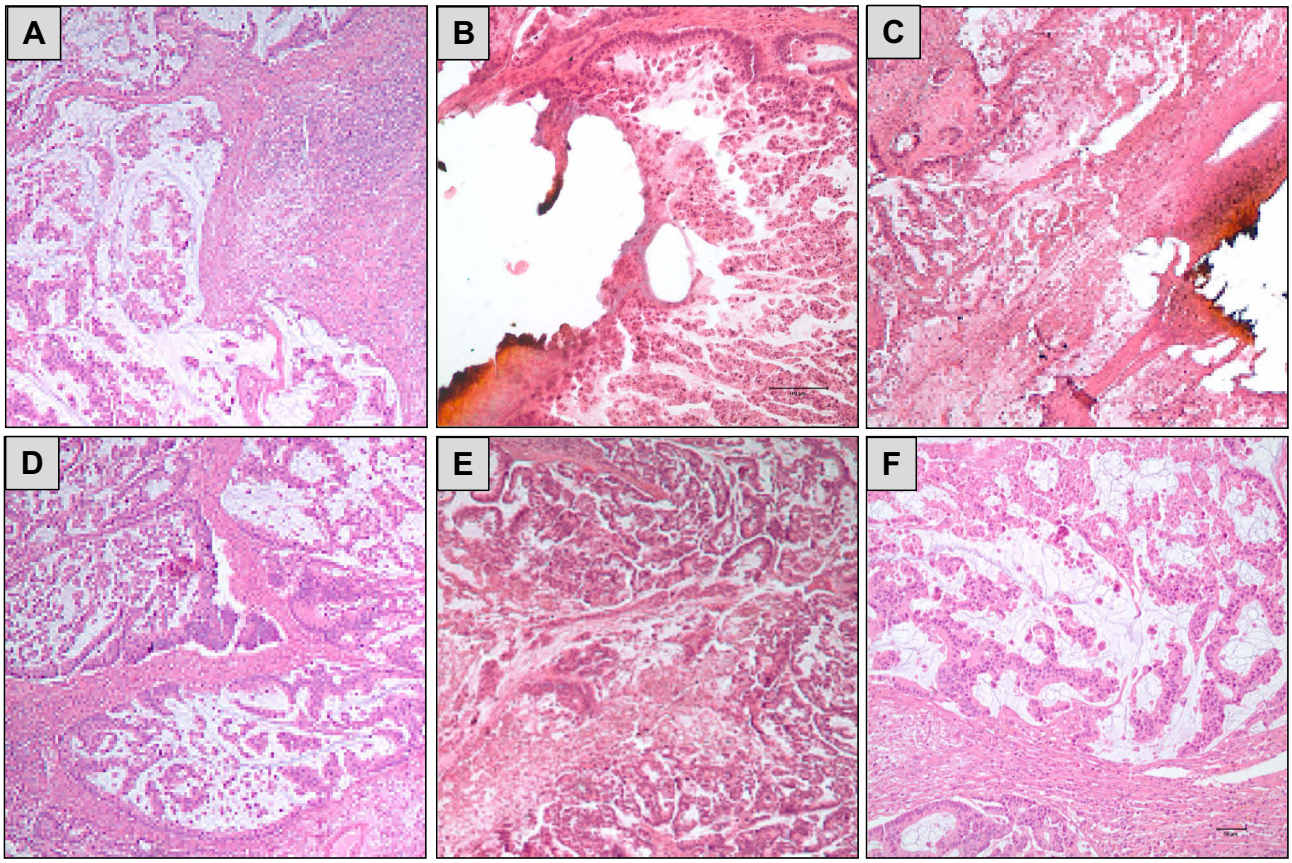

Figure 14 The pathological observations in the laser exposed tumor tissue after H&E staining; (**A**) the negative control group without laser exposure and with PGNSs (scale bar 50 µm), (**B**) 1.0 cm tissue depth with PGNSs and laser exposure (scale bar 100 µm), (**C**) 2.0 cm tissue depth with PGNSs and laser (scale bar 100 µm), (**D**) 3.0 cm tissue depth with PGNSs and laser (scale bar 10 µm), (**E**) 4.0 cm tissue depth with PGNSs and laser (scale bar 50 µm) and (**F**) pathology image of the tissue at a 4.3 cm depth (side of tissue, scale bar 50 µm).

PPTT damage. After surveying the damaging effects of PPTT using an 808-nm laser in the presence of PGNSs (chicken breast tissue), investigations continued by understanding the changing effects of PPTT in this novel tumor model (Figure 14).

Figure 14A illustrates the pathology of a negative control group neither exposed to a laser or PGNSs. Figure 14B demonstrates the structural changes created by PPTT heat damage in a tumor slice sectioned 1.0 cm inside the tissue. The microscopic pathology results identified serious degenerative damage (burn like) in the nanoparticle accumulated region. Other parts of the tumor tissue in Figure 14B were affected with heat produced by photothermally but in the form of reversible changes. Figure 14C shows the tissue changes at a depth of 2.0 cm of tissue slices. In Figure 14D, E and F, in much deeper slices (more than 3 cm), no remarkable damage was observed revealing no significant changes in tissue structure due to the laser and nanoparticle combination.

Conclusions

A new means of alternative cancer therapeutic complementary techniques called "plasmonic photothermal therapy" is emphasized here to synthesize effective nanostructures with significant improvements in regards to light and heat conversion used for cancer treatment. In the present study, efficient morphologies of gold nanoparticles termed "pimpled gold nanoparticles (PGNSs)" were formulated and studied. According to the thermography results with nanoparticles, numerical studies with nanoparticles determined electrical field enhancement (E) clearly showing the ability of a laser to convert light to heat for the PGNSs. Experimental assessment and theoretical studies (modeled using COMSOL) of the PGNSs under PPTT were conducted. Thermography experimental results of PPTT and the nanoparticle phantom identified the highest temperature change for the PGNSs group (ΔT=29.8°C) following the COMSOL numerical model. The highest cell viability percentage, when exposed to the nanoparticles (more than 93%), was determined by MTT assays at the highest concentration. PPTT results were obtained through in vitro assessment which revealed a significant apoptosis index (~70% apoptosis for PGNSs compared to 53% in AuNRs for the DLD-1 cell line). In pathological observations using an ex vivo tissue model, due to the high energy of a 532-nm laser, its penetration only reached hundreds of micrometers but induced serious damage to the region of interest. For the 808-nm laser/PGNS combination, obvious thermal damages were seen at depths higher than 2.0 cm which confirmed the robust diffusing power of an 808-laser and its interaction with PGNSs through PPTT, which can be a promising candidate for future anti-cancer medical applications with great benefits.

Acknowledgments

This study was supported by the Scientific and Technological Research Council of Turkey (TÜBİTAK) under the 1003 classification project.

Disclosure

The authors report no conflicts of interest in this work.

References

1. Feynman RP. There's plenty of room at the bottom. *Indian J Med Sci*. 1960;23:15.
2. Nour S, Baheiraei N, Imani R, et al. Bioactive materials: a comprehensive review on interactions with biological microenvironment based on the immune response. *J Bionic Eng*. 2019;16(4):563–581. doi:10.1007/s42235-019-0046-z
3. Hajebi S, Rabiee N, Bagherzadeh M, et al. Stimulus-responsive polymeric nanogels as smart drug delivery systems. *Acta Biomater*. 2019;92:1–18. doi:10.1016/j.actbio.2019.05.018
4. Nour S, Baheiraei N, Imani R, et al. A review of accelerated wound healing approaches: biomaterial-assisted tissue remodeling. *J Mater Sci*. 2019;30(10):120.
5. Farjadian F, Moghoofei M, Mirkiani S, et al. Bacterial components as naturally inspired nano-carriers for drug/gene delivery and immunization: set the bugs to work? *Biotechnol Adv*. 2018;36(4):968–985. doi:10.1016/j.biotechadv.2018.02.016
6. Vo-Dinh T. *Nanotechnology in Biology and Medicine: Methods, Devices, and Applications*. CRC Press; 2017.
7. Shi J, Kantoff PW, Wooster R, et al. Cancer nanomedicine: progress, challenges and opportunities. *Nat Rev Cancer*. 2017;17(1):20. doi:10.1038/nrc.2016.108
8. Kim KY. *Nanotechnology Platforms and Physiological Challenges for Cancer Therapeutics, in Nanomedicine in Cancer*. Pan Stanford; 2017:27–46.
9. Ferlay J, Soerjomataram I, Dikshit R, et al. Cancer incidence and mortality worldwide: sources, methods and major patterns in GLOBOCAN 2012. *Int J Cancer*. 2015;136(5):E359–E386. doi:10.1002/ijc.29210
10. Chang AY, Cowling K, Micah AE, et al. Past, present, and future of global health financing: a review of development assistance, government, out-of-pocket, and other private spending on health for 195 countries, 1995–2050. *Lancet*. 2019;393(10187):2233–2260. doi:10.1016/S0140-6736(19)30841-4
11. Zagar TM, Oleson JR, Vujaskovic Z, et al. Hyperthermia for locally advanced breast cancer. *Int J Hyperthermia*. 2010;26(7):618–624. doi:10.3109/02656736.2010.501051
12. Kim JH, Hahn EW, Ahmed SA. Combination hyperthermia and radiation therapy for malignant melanoma. *Cancer*. 1982;50(3):478–482. doi:10.1002/1097-0142(19820801)50:3<478::AID-CNCR2820500316>3.0.CO;2-6
13. Fisher B, Redmond C, Poisson R, et al. 8-year results of a randomized clinical-trial comparing total mastectomy and lumpectomy with or without irradiation in the treatment of breast-cancer. *N Engl J Med*. 1989;320(13):822–828. doi:10.1056/NEJM198903303201302

14. Füzéry AK, Levin J, Chan MM, et al. Translation of proteomic biomarkers into FDA approved cancer diagnostics: issues and challenges. *Clin Proteomics*. 2013;10(1):13. doi:10.1186/1559-0275-10-13
15. Depciuch J, Stec M, Kandler M, et al. From spherical to bone-shaped gold nanoparticles—Time factor in the formation of Au NPs, their optical and photothermal properties. *Photodiagnosis Photodyn Ther*. 2020;30:101670. doi:10.1016/j.pdpdt.2020.101670
16. Depciuch J, Stec M, Maximenko A, et al. Gold nanodahlias: potential nanophotosensitizer in photothermal anticancer therapy. *J Mater Sci*. 2020;55(6):2530–2543. doi:10.1007/s10853-019-04187-z
17. Saw WS, Ujihara M, Chong WY, et al. Size-dependent effect of cystine/citric acid-capped confeito-like gold nanoparticles on cellular uptake and photothermal cancer therapy. *Colloids Surf B Biointerfaces*. 2018;161:365–374. doi:10.1016/j.colsurfb.2017.10.064
18. Yang H, He H, Tong Z, et al. The impact of size and surface ligand of gold nanorods on liver cancer accumulation and photothermal therapy in the second near-infrared window. *J Colloid Interface Sci*. 2020;565:186–196. doi:10.1016/j.jcis.2020.01.026
19. Aioub M, Panikkanvalappil SR, El-Sayed MA. Platinum-coated gold nanorods: efficient reactive oxygen scavengers that prevent oxidative damage toward healthy, untreated cells during plasmonic photothermal therapy. *ACS Nano*. 2017;11(1):579–586. doi:10.1021/acsnano.6b06651
20. Parchur AK, Sharma G, Jagtap JM, et al. Vascular interventional radiology-guided photothermal therapy of colorectal cancer liver metastasis with theranostic gold nanorods. *ACS Nano*. 2018;12(7):6597–6611. doi:10.1021/acsnano.8b01424
21. Yu Y, Zhou M, Zhang W, et al. Rattle-type gold Nanorods/Porous-SiO 2 nanocomposites as near-infrared light-activated drug delivery systems for cancer combined chemo–photothermal therapy. *Mol Pharm*. 2019;16(5):1929–1938. doi:10.1021/acs.molpharmaceut.8b01298
22. Yan J, Sun H, Li J, et al. A theranostic plaster combining photothermal therapy and photodynamic therapy based on chlorin e6/gold nanorods (Ce6/Au nrs) composite. *Colloids Surf a Physicochem Eng Asp*. 2018;537:460–466. doi:10.1016/j.colsurfa.2017.10.051
23. Lee S-Y, Shieh M-J. Platinum (II) drug-loaded gold nanoshells for chemo-photothermal therapy in colorectal cancer. *ACS Appl Mater Interfaces*. 2020.
24. Sharma AK, Pandey S, Khan MS, et al. Protein stabilized fluorescent gold nanocubes as selective probe for alkaline phosphatase via inner filter effect. *Sens Actuators B Chem*. 2018;259:83–89. doi:10.1016/j.snb.2017.11.190
25. Hernández Y, Galarreta BC. *Noble Metal-Based Plasmonic Nanoparticles for SERS Imaging and Photothermal Therapy, in Nanomaterials for Magnetic and Optical Hyperthermia Applications*. Elsevier; 2019:83–109.
26. Wu F, Liu Y, Wu Y, et al. Chlorin e6 and polydopamine modified Gold nanoflowers for combined photothermal and photodynamic therapy. *J Mater Chem B*. 2020;8(10):2128–2138. doi:10.1039/C9TB02646K
27. Dreaden EC, Alkilany AM, Huang X, et al. The golden age: gold nanoparticles for biomedicine. *Chem Soc Rev*. 2012;41(7):2740–2779.
28. Swearer DF, Leary RK, Newell R, et al. Transition-metal decorated aluminum nanocrystals. *ACS Nano*. 2017;11(10):10281–10288. doi:10.1021/acsnano.7b04960
29. Bao C, Beziere N, Del Pino P, et al. Gold nanoprisms as optoacoustic signal nanoamplifiers for in vivo bioimaging of gastrointestinal cancers. *Small*. 2013;9(1):68–74. doi:10.1002/smll.201201779
30. Liu N, Tang ML, Hentschel M, et al. Nanoantenna-enhanced gas sensing in a single tailored nanofocus. *Nat Mater*. 2011;10(8):631. doi:10.1038/nmat3029
31. Chen Y, Zhang Y, Pan F, et al. Breath analysis based on surface-enhanced Raman scattering sensors distinguishes early and advanced gastric cancer patients from healthy persons. *ACS Nano*. 2016;10(9):8169–8179. doi:10.1021/acsnano.6b01441
32. Sailor MJ, Park JH. Hybrid nanoparticles for detection and treatment of cancer. *Adv Mater*. 2012;24(28):3779–3802. doi:10.1002/adma.201200653
33. Ashley CE, Carnes EC, Phillips GK, et al. The targeted delivery of multicomponent cargos to cancer cells by nanoporous particle-supported lipid bilayers. *Nat Mater*. 2011;10(5):389. doi:10.1038/nmat2992
34. Bao C, Conde J, Pan F, et al. Gold nanoprisms as a hybrid in vivo cancer theranostic platform for in situ photoacoustic imaging, angiography, and localized hyperthermia. *Nano Res*. 2016;9(4):1043–1056. doi:10.1007/s12274-016-0996-y
35. Zhang C, Li C, Liu Y, et al. Gold nanoclusters-based nanoprobes for simultaneous fluorescence imaging and targeted photodynamic therapy with superior penetration and retention behavior in tumors. *Adv Funct Mater*. 2015;25(8):1314–1325. doi:10.1002/adfm.201403095
36. Gao Y, Li Y, Wang Y, et al. Controlled synthesis of multilayered gold nanoshells for enhanced photothermal therapy and SERS detection. *Small*. 2015;11(1):77–83. doi:10.1002/smll.201402149
37. Ke H, Yue X, Wang J, et al. Gold nanoshelled liquid perfluorocarbon nanocapsules for combined dual modal ultrasound/CT imaging and photothermal therapy of cancer. *Small*. 2014;10(6):1220–1227. doi:10.1002/smll.201302252
38. Abadeer NS, Murphy CJ. Recent progress in cancer thermal therapy using gold nanoparticles. *J Phys Chem C*. 2016;120(9):4691–4716. doi:10.1021/acs.jpcc.5b11232
39. Abadeer NS, Brennan MR, Wilson WL, et al. Distance and plasmon wavelength dependent fluorescence of molecules bound to silica-coated gold nanorods. *ACS Nano*. 2014;8(8):8392–8406. doi:10.1021/nn502887j
40. Jain PK, Lee KS, El-Sayed IH, et al. Calculated absorption and scattering properties of gold nanoparticles of different size, shape, and composition: applications in biological imaging and biomedicine. *J Phys Chem B*. 2006;110(14):7238–7248. doi:10.1021/jp057170o
41. Liu H, Liu T, Wu X, et al. Targeting gold nanoshells on silica nanorattles: a drug cocktail to fight breast tumors via a single irradiation with near-infrared laser light. *Adv Mater*. 2012;24(6):755–761. doi:10.1002/adma.201103343
42. Huang Y, Wei T, Yu J, et al. Multifunctional metal rattle-type nanocarriers for MRI-guided photothermal cancer therapy. *Mol Pharm*. 2014;11(10):3386–3394. doi:10.1021/mp500006z
43. Godavarty A, Rodriguez S, Jung YJ, Gonzalez S. Optical imaging for breast cancer prescreening. *Breast Cancer*. 2015;7:193.
44. Meyer-Schwickerath G. Erfahrungen mit der Lichtkoagulation der Netzhaut und der Iris. *Doc Ophthalmol*. 1956;10(1):91–131. doi:10.1007/BF00172100
45. Boas DA, Brooks DH, Miller EL, et al. Imaging the body with diffuse optical tomography. *IEEE Signal Process Mag*. 2001;18(6):57–75. doi:10.1109/79.962278
46. Turkevich J, Stevenson PC, Hillier J. The formation of colloidal gold. *J Phys Chem*. 1953;57(7):670–673. doi:10.1021/j150508a015
47. Nikoobakht B, El-Sayed MA. Preparation and growth mechanism of gold nanorods (NRs) using seed-mediated growth method. *Chemi Mater*. 2003;15(10):1957–1962. doi:10.1021/cm0207321
48. Duff DG, Baiker A, Edwards PP. A new hydrosol of gold clusters 0.1. Formation and particle-size variation. *Langmuir*. 1993;9(9):2301–2309. doi:10.1021/la00033a010
49. Fan R-J, Sun Q, Zhang L, et al. Photoluminescent carbon dots directly derived from polyethylene glycol and their application for cellular imaging. *Carbon*. 2014;71:87–93. doi:10.1016/j.carbon.2014.01.016
50. Ziegler C, Eychmuller A. Seeded growth synthesis of uniform gold nanoparticles with diameters of 15-300 nm. *J Phys Chem C*. 2011;115(11):4502–4506. doi:10.1021/jp1106982